5-1-2021

Impact of Squeezing on the Microstructure of Thermal Interface Materials

R. Kantharaj

C. Wassgren

A. Morris

A. M. Marconnet

Kantharaj, R.; Wassgren, C.; Morris, A.; and Marconnet, A. M., "Impact of Squeezing on the Microstructure of Thermal Interface Materials" (2021). *CTRC Research Publications.* Paper 420.
http://dx.doi.org/https://doi.org/10.1109/ITherm51669.2021.9503232

2021 20th IEEE Intersociety Conference on Thermal and Thermomechanical Phenomena in Electronic Systems (iTherm) | 978-1-7281-8539-2/21/$31.00 ©2021 IEEE | DOI: 10.1109/ITherm51669.2021.9503232

Impact of Squeezing on the Microstructure of Thermal Interface Materials

Rajath Kantharaj
School of Mechanical Engineering
Purdue University
West Lafayette, USA
rkanthar@purdue.edu

Carl Wassgren
School of Mechanical Engineering
Purdue University
West Lafayette, USA
wassgren@purdue.edu

Aaron Morris
School of Mechanical Engineering
Purdue University
West Lafayette, USA
morri353@purdue.edu

Amy Marconnet
School of Mechanical Engineering
Purdue University
West Lafayette, USA
amarconn@purdue.edu

***Abstract*—Thermal interface materials (TIMs), consisting of high conductivity filler particles dispersed in a polymer matrix, are used in thermal management of electronics to bridge the gap between the heat generating components and the heat spreader or heat sink. Without TIMs, there is imperfect contact at the interface, resulting in detrimental chip performance and elevated temperatures that can ultimately lead to failure of the chip. In commercial applications, TIMs are dispensed on the chip, heat spreader, or the heat sink using a nozzle via an automated process. The TIM is then squeezed into a thin layer over the substrate by the alternate component (*i.e.*, the device, heat spreader, or the heat sink), often followed by curing (*e.g.*, at elevated temperature) to form a rigid bond. During squeezing, the particle-laden TIM generally exhibits non-Newtonian behavior and, after squeezing, the particle spatial distribution may be non-uniform. The flow behavior depends on dispense pattern (*e.g.*, dots, lines, star patterns), parameters of the squeezing process (*e.g.*, force and squeezing rate), and the TIM composition (*e.g.*, particle shape, size distribution, volume fraction, and matrix composition). The velocity and applied pressure during squeezing significantly impacts the achievable bond line thickness (BLT) and the particle spatial distribution, which can cause the thermal performance of the TIM to deviate from the vendor-specified thermal characteristics. In practice, the maximum allowable squeeze pressure, which impacts the final BLT, is limited by potential mechanical failure of packaged electronics. There are open questions regarding the effect of squeezing on particle rearrangement and its effect on thermal conduction within the particle network. In this work, X-ray micro-computed tomography (XRCT) is used to measure the spatial distribution of particles in the TIM after (a) dispensing and (b) squeezing processes. A mock TIM with a target of 30 vol% copper microspheres (median diameter 114 µm) is created by hand-mixing the particles with a UV-curable epoxy. Microstructural features such as the average particle volume fraction, coordination number and radial distribution function (RDF) are computed to gain insights into the particle spatial arrangement in the TIM.**

Keywords—particle laden polymeric TIMs, squeezing-induced particle heterogeneity, X-ray micro computed tomography, microstructure analysis of dispensed and squeezed TIMs

I. Introduction

Modern microprocessors have more than 10 billion transistors, each with a characteristic size of about 7 nm [1]. These transistors are packed in a small footprint or die area. As of 2015, the heat flux dissipated in a commercial processor exceeds 100 W cm^{-2} [2], with localized hot spots reaching heat fluxes greater than 1 kW cm^{-2} [3]. If the heat is not dissipated efficiently, the internal temperature of the chip reaches temperatures that reduce the microchip efficiency and decrease its lifetime. Interfaces between (a) the microprocessor chip and lid and (b) the lid and heat sink tend to have poor thermal transport due to roughness that limits contact between the surfaces. Indeed, the typical contact area for dry mating surfaces is on the order of $1-2$ % of the nominal (or apparent) cross-sectional area of the mating objects [4]. This small contact area leads to a high interface thermal resistance and a large temperature drop across the heat flow path. Since temperature rises across interfaces can contribute up to 50% of the total temperature increase [5], decreasing the thermal contact resistance at these interfaces is important for improving microchip performance.

Thermal interface materials (TIMs) aid in efficient heat conduction across interfaces and numerous materials have been developed for this purpose, including greases, gels, epoxies, and phase change materials. Current research often focuses on TIMs consisting of high thermal conductivity particles immersed in a curable polymer matrix that form a rigid bond. These materials are sometimes called "thermally conductive adhesives" or "thermal epoxies". Prasher [4] extensively reviewed these composite polymeric TIMs and their rheology and design was investigated by Prasher *et al*. [6,7]. In the TIMs, the particle volume fraction (or filler loading) is usually greater than 50% [4,8]. On an industrial assembly line, the TIM is generally (i) dispensed in a viscous state onto the substrate with a controlled flow rate and/or quantity and then (ii) squeezed with either constant velocity [9] or force [10] to achieve the desired final pressure or desired bond line thickness (BLT). Various dispense patterns (such as dots, lines, spirals, serpentine, "X" shaped, and star patterns) and different protocols for the squeeze process have been tested with the goal of optimizing uniformity of the final TIM. Typical pressures when squeezing the TIM range from $5-150$ psi (34.5 kPa $-$ 1 MPa) [4,5,7,10–15]. An exception is the work of Rae *et al.* [9] in which a pressure of ~2.5 MPa was applied.

During squeezing, the filler particles and polymer matrix can flow relative to each other, and this relative movement can modify the TIM microstructure as compared to its dispensed state. The final microstructure, *i.e.*, the arrangement of the filler particles, might not be uniform, impacting thermal performance during operation. Only a few works [9,10,16] have recognized the relationship between the nature of squeeze flow, evolution

We thank the Cooling Technologies Research Center (CTRC), a graduated National Science Foundation Industry/University Cooperative Research Center at Purdue University, for providing funding for this project

of TIM microstructure during squeeze, and the effective thermal conductivity of the squeezed TIM. Of these, only Rae *et al.* [9] made an effort to visualize the TIM particle networks at high resolution after squeezing. In their work, a commercial TIM was squeezed at constant velocity, ranging from $0.1 - 10\ \mu m\ s^{-1}$, to an ultimate squeeze pressure of $\sim 2.5\ MPa$. Relatively small squeeze velocities lead to significant separation of the particles and polymer matrix leading to a heterogeneous microstructure. This non-uniform packing of particles also impacts the minimum achievable BLT and the overall effective thermal resistance of the interface. Note that in the work by Rae *et al.* [9] the TIM was cured in two different ways after squeezing: with and without the critical squeeze force held on the material. Fast squeezing and curing with the squeeze force held on the TIM led to a more homogeneous distribution of particles within the TIM and lowered the BLT and thermal resistance compared to slow squeezing and curing without the force. The bulk thermal resistance was approximately a half order of magnitude smaller when compared with slow squeezing followed by curing without the compressive force. While this work shows the impact of squeezing parameters on the microstructure and performance, there is a lack of quantitative analysis of the 3D microstructure and its impact on macroscopic properties such as thermal conductivity.

Migration of the liquid phase or matrix filtration (here, the polymer matrix) in particulate suspensions, including pastes or granular suspensions [17–21], has been observed in petrochemical applications [22] and water filtration in sewage [23]. A large local concentration of the particles arises as a result of the separation of liquid and solid phases during squeezing [24]. A rigorous mathematical treatment can be found in Poitou and Racineux [21]. Briefly, the critical squeeze velocity below which matrix filtration occurs is a function of the particle size (D_p), particle volume fraction (ϕ_s), matrix dynamic viscosity (μ_f), and the fluid flow characteristics such as yield stress, flow index, and consistency [21,22,25]. Experimentally, the localized high concentration of particles during slow squeezing, as a result of matrix filtration, was observed by Shirazy *et al.* [10] for two different TIMs with "extremely high" and "high" particle volume fractions. In their work, a constant squeeze force rate was employed to study the particle distribution. Based on these past works, it is clear that the same TIM formulation can yield varying degrees of homogeneity depending on the application conditions resulting in non-uniform local thermal resistances and variations in the overall thermal resistance.

Depending on the dispense pattern and squeeze velocity (or squeeze force), particle redistribution within the TIM can be severe, leaving large void or pore spaces that impede heat conduction through the material. Ultimately, the final thermal performance of the TIM is governed by the TIM application process; therefore, understanding the squeeze flow behavior of TIMs and its effects on the rearrangement or redistribution of the particle network is critical in order to optimize the dispense and squeeze processes. Prior work, such as the study by Kanuparthi *et al.* [26], predicted TIM thermal performance using microstructures generated from algorithms such as drop-fall-shake that did not include the application process or particle-matrix interactions. While the final volume fraction of particles matches experiments, the microstructure may not be accurate. The squeezing process and the heat transfer performance of TIMs have also been modeled using the thermal Lattice-Boltzmann method [27]. For instance, Khiabani *et al.* [27] modeled a constant pressure squeeze process assuming a uniform initial distribution of particles within the polymer matrix. This assumption neglects the true initial particle distribution and the shape of the dispense pattern, such as heap-like lines, dots, or stars. Experimental data for the particle locations after dispensing is needed to provide more accurate starting configurations for TIM microstructure modeling and thermal calculations.

In this work, we experimentally investigate the TIM microstructure after dispensing and after squeezing to understand the arrangement of the particles and the impact of squeezing parameters. We synthesize mock TIMs, consisting of relatively-large, nearly-spherical high thermal conductivity (copper) filler particles in a UV-curable matrix. The dispensed and squeezed TIMs are analyzed using X-ray micro computed tomography (XRCT) to identify the particle locations and diameters in both states. The volume fraction, coordination number and radial distribution function are used to quantify the TIM microstructure. These data provide a starting point for validating models predicting microstructure and TIM thermal performance.

II. Experimental Methodology

A. Sample Fabrication

A mock TIM is prepared by manually mixing spherical copper particles (Cu powder 150um spherical, Stock # US5002, purchased from US Research Nanomaterials, Inc,) with a UV-curable epoxy (UV Cure 60-7158, purchased from Epoxies, Etc.) with a target particle volume fraction of 30%. The as-received particles are sieved to work with particle sizes of $90 - 125\ \mu m$ with a median diameter of $\sim 114\ \mu m$. Copper particles have high thermal conductivity, similar to the vast majority of the commercial TIMs that commonly use ceramic, metal, or carbon-based particles [28], and provide a sufficient density difference, $\sim$8x compared to the matrix, for high contrast XRCT imaging.

Note that this mock TIM varies from commercial TIMs (larger particle sizes, UV-curable matrix, and a lower volume fraction of particles), but provides a starting point for developing experimental capabilities and validating models. We chose a lower volume fraction to speed the curing process. Combined with the UV-curing (instead of thermal curing), this short curing time minimizes particle settling, which is important for capturing the dispensed state accurately. Commercial TIMs often include variety of particles with sizes ranging from submicron to $\sim 50\ \mu m$ and can include both spherical and faceted shapes. Here, the spherical particle shape and larger particle diameter, combined with lower volume

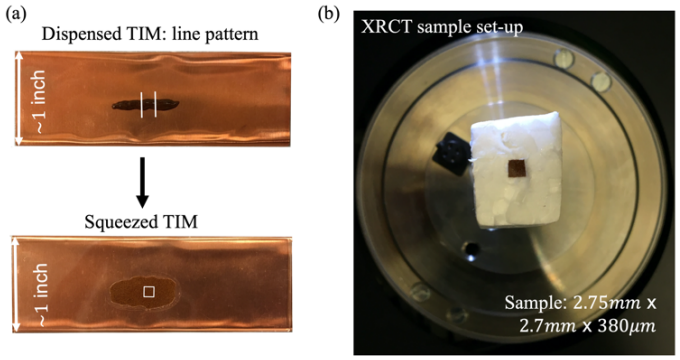

Fig. 1. Images of **(a)** the dispensed and squeezed TIMs and **(b)** the squeezed TIM sample in the Bruker SKYSCAN 1272 XRCT machine. The mock TIM consists of copper particles in a UV-curable epoxy. An isolated line pattern of the TIM is manually dispensed on a glass slide covered with copper foil (top image) and then squeezed with a second glass slide (bottom image). Samples are cut from the dispensed and squeezed TIMs. The parallel white lines in the dispensed TIM image and the white square (approximately 2.75 mm x 2.7 mm x 380 μm) in the squeezed TIM image show the approximate region from where a sample was obtained. Panel **b** shows the XRCT imaging set-up for the sample obtained in **a**. The sample is affixed to a Styrofoam support with Parafilm to prevent sample movement as it rotates during imaging. The axis of rotation is through the plane in the image shown, a conical beam of X-rays (source not shown) bombards the sample from the left and a detector on the right (not shown) collects the transmitted radiation.

fractions, improve detection and ease of analysis of individual particles via XRCT imaging.

In this study, an isolated line of TIM is dispensed on a substrate, which consisted of a microscope glass slide covered with copper foil, through a syringe with a needle opening diameter of 838 μm (or $\approx 7.4D_p$). The isolated line pattern provides insights into the fundamentals of the squeezing process as a starting point to understanding more complicated dispensed shapes. The copper foil mimics the metallic heat spreader surface found in electronics packaging. Subsequently, another bare microscope glass slide is pressed on to the dispensed TIM to manually squeeze it. The two samples are then cured for ~7.5 minutes using a 400 W metal halide UV flood lamp. This lamp illuminates an area of 0.2 x 0.2 m^2 (8 x 8 sq. inches) at an irradiance of 800 Wm^{-2}. Fig. 1 shows the UV-cured dispensed and squeezed TIM materials and a sample cut out from near the center of the squeezed TIM for 3D XRCT imaging.

B. X-ray Micro Computed Tomography (XRCT) Analysis

X-ray computed tomography (XRCT) is a non-destructive imaging technique that enables high resolution 3D imaging of samples [29]. The basic principle of this technique involves bombarding the object of interest with X-rays to collect a set of 2D projections (or raw images) as the object rotates. A detector analyzes the intensity distribution of X-rays through the object based on transmitted radiation. From the set of projections, object cross-sections can be reconstructed [30] and stacked for 3D visualization. This technique is useful in applications ranging from engineering to biomedical sciences including heterogeneous material microstructure in battery electrodes [31–33], crack growth studies [34], energy research [35], food science [36], pharmaceutical studies [37,38], and investigations of trabecular bone structure [39,40]. Applied to porous media, this technique has improved predictions of effective media properties from microstructural characteristics [41–44].

In this work, the focus is solely on TIMs consisting of spherical particles, and 3D XRCT imaging is used to experimentally analyze the microstructure of dispensed and squeezed TIMs. Both states are analyzed to provide an understanding of the microstructural changes as a result of squeezing. A Bruker SKYSCAN 1272 machine is used for 3D XRCT imaging at a voxel resolution of ~1.9 x 1.9 x 1.9 $(\mu m)^3$. Samples are scanned through 180° at a rotation step of 0.15 °. The X-ray source was set to 100 kV at a power of 10 W and a 0.11 mm thick copper filter was used. The X-ray spot size in this machine is < 5 μm. The material cross-sections are reconstructed by importing the raw images or projections from the XRCT scan to NRecon reconstruction software (Bruker). Stacking the reconstructed cross-sections enables 3D visualization of the dispensed and squeezed TIMs (see Fig. 2). CTVox (Bruker) software enables visualization of the TIM microstructure in 3D.

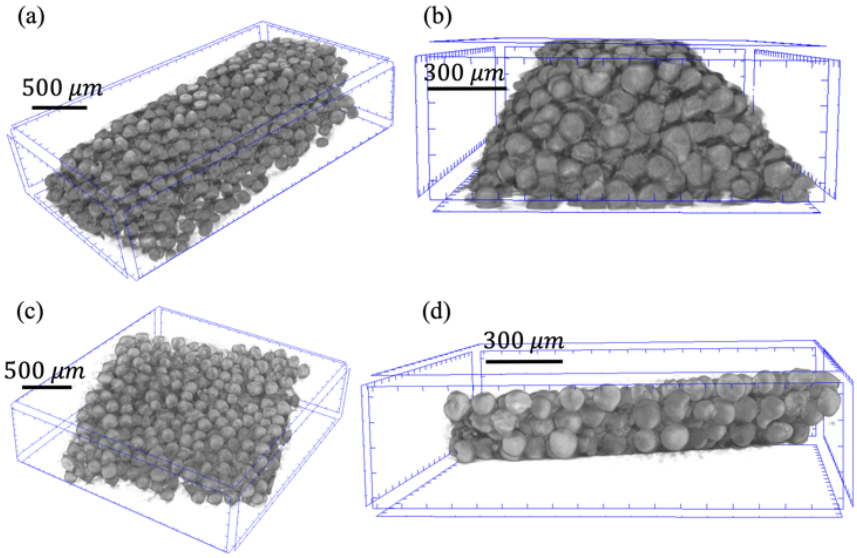

Fig. 2. **(a, b)** Dispensed and **(c, d)** squeezed TIM microstructures. The heap-like structure of the dispensed line pattern is distinctly visible in the front view (panel (b)). The squeezed TIM is approximately ~2.6 particles thick with a bond line thickness of ~297 μm. The BLT is determined using a tight-fitting box around the microstructure. The voxel resolution from the XRCT imaging is ~1.9 x 1.9 x 1.9 $(\mu m)^3$

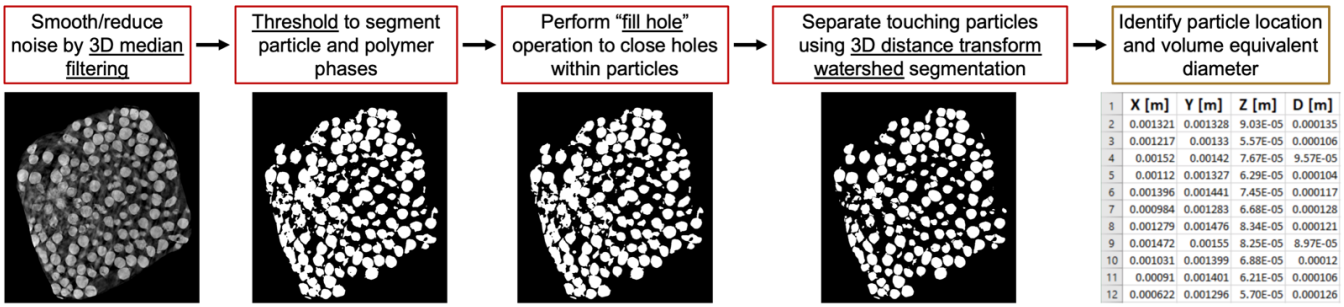

	X [m]	Y [m]	Z [m]	D [m]
2	0.001321	0.001328	9.03E-05	0.000135
3	0.001217	0.00133	5.57E-05	0.000106
4	0.00152	0.00142	7.67E-05	9.57E-05
5	0.00112	0.001327	6.29E-05	0.000104
6	0.001396	0.001441	7.45E-05	0.000117
7	0.000984	0.001283	6.68E-05	0.000128
8	0.001279	0.001476	8.34E-05	0.000121
9	0.001472	0.00155	8.25E-05	8.97E-05
10	0.001031	0.001399	6.88E-05	0.00012
11	0.00091	0.001401	6.21E-05	0.000106
12	0.000622	0.001296	5.70E-05	0.000126

Fig. 3. Flow chart illustrating the 3D image processing algorithm used to measure particle locations and sizes from XRCT images. Particle size is the equivalent sphere volume diameter calculated from the volume of connected 3D regions in the processed image after applying the distance transform watershed algorithm. Light colors indicate the particle phase, dark colors indicate the matrix (and Styrofoam holder). The images are approximately 1.88 mm x 2.03 mm.

C. 3D Image Processing

After capturing the XRCT images, the particle locations and size information must be extracted from the 3D images to quantify microstructural features such as average particle volume fraction (ϕ_s), coordination number (C_N), and the radial distribution function (RDF). Particle diameters and location are sufficient information for the microstructural analysis because the particles are approximated as spherical. We use an open-source image processing package (FIJI [45] with open source built-in algorithms and plug-ins) to process the stack of cross-sectional images of dispensed and squeezed TIMs. First, reconstructed cross-sections are loaded and, for several of the individual images, we select user-defined regions of interest (ROI) within the boundary of the TIM cross-section. These ROIs stacked together then constitute the volume of interest (VOI). Regions outside the VOI are excluded from analysis. As illustrated in Fig. 3, first noise is reduced/removed from the gray scale data by using a 3D median filter (3D Fast Filters from the 3D ImageJ plugins suite [46]) using a structural element of size ~5% of the median particle diameter. Second, a 3D auto thresholding (Otsu's method) method is used to binarize the data (black for the polymer matrix and white for particles). Third, artifacts such as holes within particles are removed through a "fill hole" operation (from the MorphoLibJ plugin [47]). Fourth, touching particles are separated, segmented, or broken artificially using the 3D distance transform watershed algorithm (available in the MorphoLibJ suite). Finally, particle centers and sizes (i.e., equivalent sphere volume diameter) are identified using the 3D Objects Counter plugin (originally published in Bolte and Cordelières [48]).

III. TIM Microstructure Analysis

In this section, the 3D image processing algorithm is validated by comparing particle sizes from the XRCT images to an alternate measurement of the particle size distribution. Microstructural features such as average particle volume fraction (ϕ_s), coordination number (C_N), and radial distribution function (RDF) are then analyzed using the particle size and location information obtained from the processed XRCT images.

A. TIM Microstructure Visualization

The particle locations and sizes measured from the 3D image processing procedure are visualized using the open-source software ParaView [49] (see Fig. 4). The XRCT imaging and image analysis are validated by comparing the imaged particle size distribution with measurements made using a Malvern Mastersizer 3000 laser-diffraction particle size analyzer. In the Malvern Mastersizer, light scattering theory is used to estimate the equivalent sphere volume diameter assuming that the particles are nearly spherical, which is a good approximation of the copper particles. In the XRCT imaging technique, particle volume is first calculated by processing the reconstructed cross-sections of the mock TIM (see Fig. 3) and then the equivalent sphere volume diameter is calculated. TABLE I. shows the D10, D50 (median), and D90 particle diameters from the laser diffraction measurement compared to those from the 3D XRCT images. Fig. 4(c) shows the normalized volume distribution (the area under the curve is equal to one) of particle sizes. There is good agreement between the two size distribution methods. In this work, the TIM was prepared from one batch of the copper particles while the size distribution was measured with a separate set of particles. The copper particles were mechanically sieved and measured with the Mastersizer. Ideally, the same batch of particles would be mixed with epoxy to prepare the TIM, but that is not feasible as the particle size distribution measurement technique is destructive.

The XRCT-measured particle sizes are expected to be slightly different than the laser diffraction particle size measurements. The "fill hole" operation in the image processing does not close all holes in the image stack and, thus, the equivalent sphere volume diameter can be underestimated

TABLE I. Characteristic particle sizes analyzed from the laser diffraction measurement and 3D image analysis of one sample from a manually dispensed line pattern TIM and one sample from a manually squeezed TIM. The "D" number is the particle size below which a given percentage (e.g., 10% for D10) of particles, by volume, are present in the sample

Char. Size	Particle Diameter [μm]		
	Laser Diffraction	*XRCT*	
		Dispensed TIM	*Squeezed TIM*
D10	91.8	95.5	99.1
D50	114	110.5	115.2
D90	140	125.5	129.5

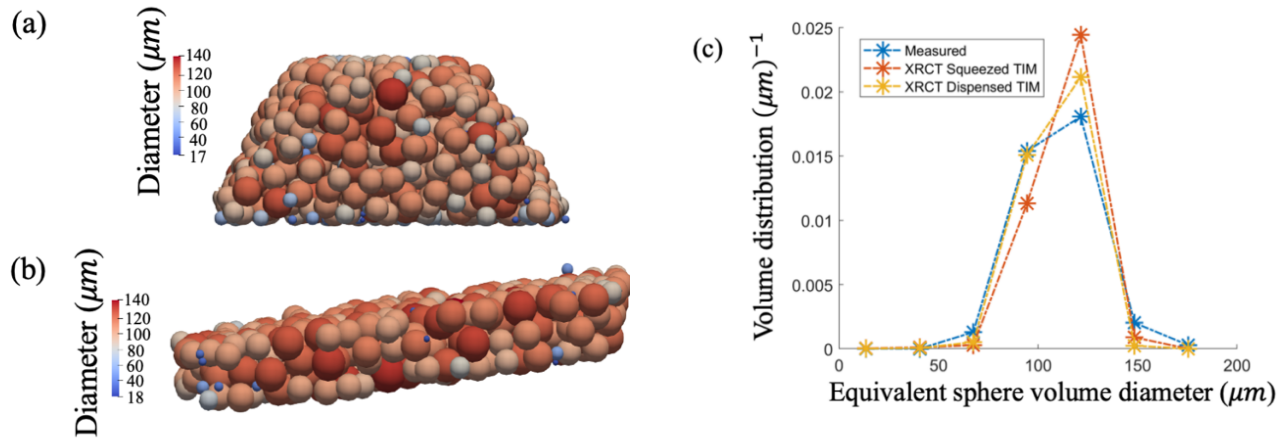

Fig. 4. Idealized 3D TIM microstructure from the detected particle locations and size (*i.e.*, equivalent sphere volume diameter) for (a) the manually dispensed line pattern TIM and (b) the manually squeezed TIM with BLT ~ 297 μm. (c) The volume distribution of particle sizes measured using laser diffraction compared to the XRCT particle size distributions for the dispensed and squeezed TIMs

TABLE II. AVERAGE PARTICLE VOLUME FRACTION (ϕ_s), COORDINATION NUMBER (C_N), AND NUMBER OF PARTICLES (N) EXTRACTED FROM THE XRCT MICROSTRUCTURE ANALYSIS OF THE DISPENSED AND SQUEEZED TIMS

TIM Sample	Application Process	ϕ_s(%)	C_N	N
Dispensed	Manually dispensed and squeezed	36.2	2.2	427
Squeezed		35.6	1.8	473

compared to the outer envelope sphere volume from the laser diffraction technique. Furthermore, image processing artefacts can cause both over- and under- estimation of the particle sizes. Over segmenting of particles through the watershed algorithm may lead to artificially smaller particle sizes, while agglomeration of multiple smaller particles due to the processing procedure combining nearby spheres could increase some particle sizes. This can explain some of the variation between the data in Fig. 4(c).

B. Microstructural Features

The *particle volume fraction*, ϕ_s, is computed by considering a tight-fitting box around the squeezed TIM microstructure analyzed from XRCT images. The squeezed sample is ~1.65 mm long in the direction along which particles redistribute during squeeze with a BLT~297 μm. In this sample, the image processing identifies 473 particles. To analyze the dispensed TIM microstructure, a rectangular subdomain is selected from within the heap-like shape of the dispensed TIM consisting of 427 particles. This subdomain is the largest rectangular region that can fit inside the dispensed TIM microstructure. Any region larger than this will contain empty space that will lead to an apparent lower volume fraction. The squeezed TIM has a slightly smaller particle volume fraction compared to the dispensed TIM. The squeezing process pushes the particles outwards, causing them to redistribute over a larger substrate area. Therefore, a slight decrease in particle volume fraction is expected. Note that for the squeezed case, a sample from near the center was cut out and that may not be representative of particle distribution characteristics over the entire TIM in the squeezed state. A better estimate of the particle volume fraction can be obtained by analyzing a rectangular sample that spans the TIM from edge-to-edge. Sampling in that manner will also provide insights into the spatial distribution of particles near and away from the centerline of the dispensed state.

The particles and epoxy were hand-mixed in a plastic beaker, which may have caused small amounts of epoxy to stick to the side of the beaker. In addition, during dispensing via a syringe needle, small amounts of epoxy may have smeared on the inner surface of the needle. These effects may have contributed to the increase in particle volume fraction in the dispensed and squeezed TIMs compared with that of mass measurements (see section IIA) prior to mixing the TIM. The key takeaway from this observation is that the TIM particle volume fraction may be modified during its application on the microprocessor or heat sink surface. TABLE II. summarizes the average particle volume fraction, coordination number, and particle number used for microstructure analysis.

The *coordination number* is computed as the mean number of geometrically intersecting pairs of particles and particle pairs that are in close proximity. In this work, an interparticle surface separation limit of 10% of the smallest radius is considered for computing the number of interacting or contacting pairs. TABLE II. shows that for both the dispensed and squeezed TIMs, on average, there are approximately two neighboring particles for a reference particle. The distribution of local contact numbers (Fig. 5) shows that there is a finite proportion of particles with greater than two neighbors in the dispensed and squeezed states. There are ~18.2% isolated particles in the squeezed state and ~13.8% in the dispensed state. From the perspective of heat conduction, the coordination number is correlated with the magnitude of heat conduction through the composite material. Isolated particles do not contribute to enhancing conduction and, therefore, their number proportion could be a metric that governs the optimal TIM application parameters. The squeezed TIM is only ~2.6 particle diameters thick and wall effects are not considered in computing the

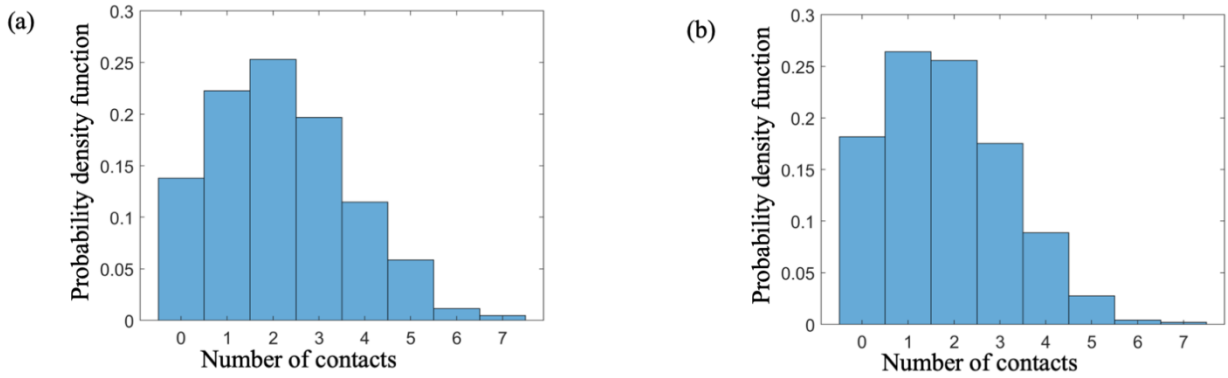

Fig. 5. Local contact number distribution in the TIM: (a) dispensed and (b) squeezed states. The mean contact number or the coordination number is 2.2 for the dispensed TIM and 1.8 for squeezed TIM. This means that, on average, a reference particle is in contact with two neighboring particles. The proportion of particles with greater than 3 contacting neighbors in the dispensed and squeezed states are respectively, 29.8% and 38.6%. Note that the proportion of isolated particles in these two states are respectively, 13.8% and 18.2%. These particles do not contribute to enhancing the heat conduction through the composite material.

coordination number. In future investigations, we intend to analyze a subset of the microstructure that consists of particles that are at least one particle diameter away from the walls.

The *radial distribution function* (RDF), or pair correlation function, represented as $g(R)$, is the probability of finding pairs of particles separated by a distance, R [50,51]. It reveals structural ordering in particulate systems [52]. The presence of sharp, well-defined peaks in the RDF suggests microstructural ordering, whereas, for disordered systems, the RDF rapidly decays to one after the first peak. For mathematical details, the reader is referred to Kirkwood and Boggs [51], Aste *et al.* [52], Franchetti [53], and Yoon *et al.* [54]. Generally, the computation of RDF exploits periodic boundary conditions, which are commonly employed in particulate systems modeling. Clearly, the experiments do not involve such boundary conditions. The finite nature of such microstructures was considered in a recent work [55], and an analytical solution was presented to calculate the RDF of finite-sized particulate microstructures. The solution involves computing the volume of intersection between a spherical shell and the bounding box for the microstructure, especially when considering reference particles near the box edges. Otherwise, the RDF artificially decays to zero. We use the freely available source code from Kopera and Retsch [55] to compute the RDF of dispensed and squeezed TIM microstructures. A search radius of 5x the maximum particle diameter and 100 bins are used to plot the RDF.

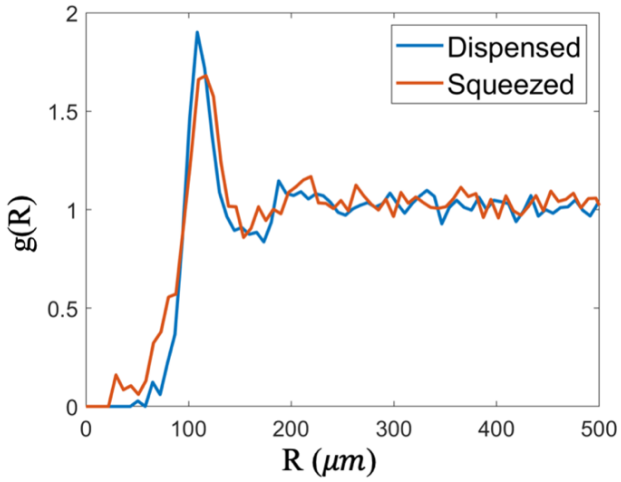

Fig. 6. RDFs of XRCT image data of single line pattern manually dispensed and manually squeezed TIMs. The search radius was 5x the maximum particle diameter and 100 bins are used for this computation. In these experimentally obtained microstructures, 427 and 473 particles are considered for dispensed and squeezed TIMs, respectively.

Fig. 6 compares the RDFs of the dispensed and squeezed TIM microstructures. The microstructures have similar spatial distributions of particles. The first peak occurs at $R_{max,1}$~112 μm for both cases and the peak is slightly taller for the dispensed TIM than the squeezed TIM. The peak radius $R_{max,1}$ closely matches with the D50 particle diameter indicating that the centers of the particles are approximately one particle diameter apart. Thereafter, the RDF fluctuates about $g(R) = 1$, suggesting a disordered microstructure.

IV. Summary and Outlook

In this work, TIM microstructures in dispensed and squeezed states were investigated using 3D XRCT imaging. Understanding squeezing-induced particle redistribution is critical to optimizing the TIM application process. Here, we focused on an isolated line dispense TIM pattern to investigate the fundamentals of particle redistribution during squeezing. Specifically, we evaluated TIMs consisting of ~114 μm spherical copper particles suspended in a UV-curable epoxy with a target volume fraction of ~30%. The particle locations and equivalent sphere volume diameter from processed XRCT data enabled quantification of the particle volume fraction (ϕ_s), coordination number (C_N), and RDF. These properties revealed that the manually dispensed and manually squeezed TIM microstructures are statistically similar. Through this work, we have established a methodology for analyzing 3D microstructures from XRCT images. Ongoing work involves (a) automation of the dispensing and squeezing processes to replicate realistic TIM application conditions, (b) XRCT imaging and microstructure analysis of the automated processed samples, (c) discrete element method (DEM)

simulations of constant velocity squeezing to predict TIM microstructure, and (d) thermal characterization and modeling. Ultimately, this work is the first step in the development of validated microstructural and thermal conduction models to guide the TIM application process with objectives of achieving uniform particle spatial distribution after squeezing and high bulk thermal conductivity.

ACKNOWLEDGMENT

We thank the Cooling Technologies Research Center (CTRC), a graduated National Science Foundation Industry/University Cooperative Research Center at Purdue University, for providing the funding for this project. I thank Seth Hogg from Micro Photonics for extensive insightful discussions on obtaining good quality X-ray micro computed tomography imaging.

REFERENCES

[1] T.M. Braun, D. Josell, J. John, and T.P. Moffat, "Simulation of Copper Electrodeposition in Through-Hole Vias," *Journal of The Electrochemical Society*, vol. 167, Oct. 2020, p. 013510, DOI:10.1149/2.0102001JES.

[2] J.L. Smoyer and P.M. Norris, "Brief Historical Perspective in Thermal Management and the Shift Toward Management at the Nanoscale," *Heat Transfer Engineering*, vol. 40, 2019, pp. 269–282, DOI:10.1080/01457632.2018.1426265.

[3] M.H. Nasr, C.E. Green, P.A. Kottke, X. Zhang, T.E. Sarvey, Y.K. Joshi, M.S. Bakir, and A.G. Fedorov, "Hotspot Thermal Management With Flow Boiling of Refrigerant in Ultrasmall Microgaps," *Journal of Electronic Packaging*, vol. 139, Mar. 2017, pp. 1–8, DOI:10.1115/1.4035387.

[4] R. Prasher, "Thermal Interface Materials: Historical Perspective, Status, and Future Directions," *Proceedings of the IEEE*, vol. 94, Aug. 2006, pp. 1571–1586, DOI:10.1109/JPROC.2006.879796.

[5] B. Smith, H. Rothuizen, R. Linderman, T. Brunschwiler, and B. Michel, "Design of thermal interfaces with embedded microchannels to control bond line formation," *2008 11th Intersociety Conference on Thermal and Thermomechanical Phenomena in Electronic Systems*, IEEE, 2008, pp. 410–418, DOI:10.1109/ITHERM.2008.4544299.

[6] R.S. Prasher, J. Shipley, S. Prstic, P. Koning, and J.-L. Wang, "Rheological Study of Micro Particle Laden Polymeric Thermal Interface Materials: Part 1 — Experimental," *Heat Transfer, Volume 7*, ASMEDC, 2002, pp. 47–51, DOI:10.1115/IMECE2002-32117.

[7] R.S. Prasher, J. Shipley, S. Prstic, P. Koning, and J.-L. Wang, "Rheological Study of Micro Particle Laden Polymeric Thermal Interface Materials: Part 2 — Modeling," *Heat Transfer, Volume 7*, ASMEDC, 2002, pp. 53–59, DOI:10.1115/IMECE2002-32118.

[8] Z. Tong, M. Liu, and H. Bao, "A numerical investigation on the heat conduction in high filler loading particulate composites," *International Journal of Heat and Mass Transfer*, vol. 100, 2016, pp. 355–361, DOI:10.1016/j.ijheatmasstransfer.2016.04.092.

[9] D.F. Rae, P. Borgesen, and E.J. Cotts, "The effect of filler-network heterogeneity on thermal resistance of polymeric thermal bondlines," *JOM*, vol. 63, Oct. 2011, pp. 78–84, DOI:10.1007/s11837-011-0180-5.

[10] M.R.S. Shirazy, S. Allard, M. Beaumier, and L.G. Frechette, "Effect of squeezing conditions on the particle distribution and bond line thickness of particle filled polymeric thermal interface materials," *Thermomechanical Phenomena in Electronic Systems - Proceedings of the Intersociety Conference*, 2014, pp. 251–259, DOI:10.1109/ITHERM.2014.6892289.

[11] R.S. Prasher, J. Shipley, S. Prstic, P. Koning, and J. Wang, "Thermal Resistance of Particle Laden Polymeric Thermal Interface Materials," *Journal of Heat Transfer*, vol. 125, 2003, p. 1170, DOI:10.1115/1.1621893.

[12] R.S. Prasher, P. Koning, J. Shipley, and A. Devpura, "Dependence of Thermal Conductivity and Mechanical Rigidity of Particle-Laden Polymeric Thermal Interface Material on Particle Volume Fraction," *Journal of Electronic Packaging*, vol. 125, 2003, p. 386, DOI:10.1115/1.1602703.

[13] R. Linderman, T. Brunschwiler, B. Smith, and B. Michel, "High-performance thermal interface technology overview," *2007 13th International Workshop on Thermal Investigation of ICs and Systems (THERMINIC)*, IEEE, 2007, pp. 129–134, DOI:10.1109/THERMINIC.2007.4451762.

[14] K.M. Razeeb, E. Dalton, G.L.W. Cross, and A.J. Robinson, "Present and future thermal interface materials for electronic devices," *International Materials Reviews*, vol. 6608, 2017, pp. 1–21, DOI:10.1080/09506608.2017.1296605.

[15] X. Hu, S. Govindasamy, and K.E. Goodson, "Two-Medium Model for the Bond Line Thickness of Particle Filled Thermal Interface Materials," *Heat Transfer, Volume 3*, ASME, 2004, pp. 337–342, DOI:10.1115/IMECE2004-62027.

[16] D.A. Davidson, G.L. Lehmann, and B.T. Murray, "Study of a gel thermal interface material with micron-size particles," *Thermal and Thermomechanical Proceedings 10th Intersociety Conference on Phenomena in Electronics Systems, 2006. ITHERM 2006.*, IEEE, 2006, pp. 497–504, DOI:10.1109/ITHERM.2006.1645385.

[17] S. Mascia and D.I. Wilson, "Rheology of concentrated granular suspensions undergoing squeeze flow," *Journal of Rheology*, vol. 51, May. 2007, pp. 493–515, DOI:10.1122/1.2716448.

[18] A. Ramachandran and D.T. Leighton, "Particle migration in concentrated suspensions undergoing squeeze flow," *Journal of Rheology*, vol. 54, May. 2010, pp. 563–589, DOI:10.1122/1.3372837.

[19] R.J. Phillips, R.C. Armstrong, R.A. Brown, A.L. Graham, and J.R. Abbott, "A constitutive equation for concentrated suspensions that accounts for shear-induced particle migration," *Physics of Fluids A: Fluid Dynamics*, vol. 4, Jan. 1992, pp. 30–40, DOI:10.1063/1.858498.

[20] J. Collomb, F. Chaari, and M. Chaouche, "Squeeze flow of concentrated suspensions of spheres in Newtonian and shear-thinning fluids," *Journal of Rheology*, vol. 48, Mar. 2004, pp. 405–416, DOI:10.1122/1.1645514.

[21] A. Poitou and G. Racineux, "A squeezing experiment showing binder migration in concentrated suspensions," *Journal of Rheology*, vol. 45, 2002, pp. 609–625, DOI:10.1122/1.1366717.

[22] F. Kolenda, P. Retana, G. Racineux, and A. Poitou, "Identification of rheological parameters by the squeezing test," *Powder Technology*, vol. 130, Feb. 2003, pp. 56–62, DOI:10.1016/S0032-5910(02)00227-9.

[23] F. Chaari, G. Racineux, A. Poitou, and M. Chaouche, "Rheological behavior of sewage sludge and strain-induced dewatering," *Rheologica Acta*, vol. 42, May. 2003, pp. 273–279, DOI:10.1007/s00397-002-0276-5.

[24] N. Delhaye, A. Poitou, and M. Chaouche, "Squeeze flow of highly concentrated suspensions of spheres," *Journal of Non-Newtonian Fluid Mechanics*, vol. 94, Nov. 2000, pp. 67–74, DOI:10.1016/S0377-0257(00)00130-0.

[25] J.D. Sherwood, "Liquid–solid relative motion during squeeze flow of pastes," *Journal of Non-Newtonian Fluid Mechanics*, vol. 104, Apr. 2002, pp. 1–32, DOI:10.1016/S0377-0257(02)00011-3.

[26] S. Kanuparthi, G. Subbarayan, T. Siegmund, and B. Sammakia, "An Efficient Network Model for Determining the Effective Thermal Conductivity of Particulate Thermal Interface Materials," *IEEE Transactions on Components and Packaging Technologies*, vol. 31, 2008, pp. 611–621, DOI:10.1109/TCAPT.2008.2001839.

[27] R.H. Khiabani, Y. Joshi, and C.K. Aidun, "Thermal properties of particulate TIMs in squeeze flow," *International Journal of Heat and Mass Transfer*, vol. 53, 2010, pp. 4039–4046, DOI:10.1016/j.ijheatmasstransfer.2010.05.023.

[28] J. Liu, B. Michel, M. Rencz, C. Tantolin, C. Sarno, R. Miessner, K.V. Schuett, X. Tang, S. Demoustier, and A. Ziaei, "Recent progress of thermal interface material research - an overview," *14th International Workshop on THERMal INvestigation of ICs and Systems, THERMINIC 2008*, 2008, pp. 156–162, DOI:10.1109/THERMINIC.2008.4669900.

[29] S.R. Stock, "X-ray microtomography of materials," *International Materials Reviews*, vol. 44, Apr. 1999, pp. 141–164, DOI:10.1179/095066099101528261.

[30] V. BUSIGNIES, B. LECLERC, P. PORION, P. EVESQUE, G. COUARRAZE, and P. TCHORELOFF, "Quantitative measurements of localized density variations in cylindrical tablets using X-ray microtomography," *European Journal of Pharmaceutics and Biopharmaceutics*, vol. 64, Aug. 2006, pp. 38–50, DOI:10.1016/j.ejpb.2006.02.007.

[31] A. Yermukhambetova, C. Tan, S.R. Daemi, Z. Bakenov, J.A. Darr, D.J.L. Brett, and P.R. Shearing, "Exploring 3D microstructural evolution in Li-Sulfur battery electrodes using in-situ X-ray tomography," *Scientific Reports*, vol. 6, 2016, pp. 1–9, DOI:10.1038/srep35291.

[32] A. Etiemble, J. Adrien, E. Maire, H. Idrissi, D. Reyter, and L. Roué, "3D morphological analysis of copper foams as current collectors for Li-ion batteries by means of X-ray tomography," *Materials Science and Engineering: B*, vol. 187, Sep. 2014, pp. 1–8, DOI:10.1016/j.mseb.2014.04.006.

[33] M. Ebner, F. Geldmacher, F. Marone, M. Stampanoni, and V. Wood, "X-Ray Tomography of Porous, Transition Metal Oxide Based Lithium Ion Battery Electrodes," *Advanced Energy Materials*, vol. 3, Jul. 2013, pp. 845–850, DOI:10.1002/aenm.201200932.

[34] E. Maire and P.J. Withers, "Quantitative X-ray tomography," *International Materials Reviews*, vol. 59, 2014, pp. 1–43, DOI:10.1179/1743280413Y.0000000023.

[35] N.R. Backeberg, F. Iacoviello, M. Rittner, T.M. Mitchell, A.P. Jones, R. Day, J. Wheeler, P.R. Shearing, P. Vermeesch, and A. Striolo, "Quantifying the anisotropy and tortuosity of permeable pathways in clay-rich mudstones using models based on X-ray tomography," *Scientific Reports*, vol. 7, Dec. 2017, p. 14838, DOI:10.1038/s41598-017-14810-1.

[36] E. Herremans, P. Verboven, B.E. Verlinden, D. Cantre, M. Abera, M. Wevers, and B.M. Nicolaï, "Automatic analysis of the 3-D microstructure of fruit parenchyma tissue using X-ray micro-CT explains differences in aeration," *BMC Plant Biology*, vol. 15, Dec. 2015, p. 264, DOI:10.1186/s12870-015-0650-y.

[37] I.C. Sinka, S.F. Burch, J.H. Tweed, and J.C. Cunningham, "Measurement of density variations in tablets using X-ray computed tomography," *International Journal of Pharmaceutics*, vol. 271, Mar. 2004, pp. 215–224, DOI:10.1016/j.ijpharm.2003.11.022.

[38] J. ZEITLER and L. GLADDEN, "In-vitro tomography and non-destructive imaging at depth of pharmaceutical solid dosage forms," *European Journal of Pharmaceutics and Biopharmaceutics*, vol. 71, Jan. 2009, pp. 2–22, DOI:10.1016/j.ejpb.2008.08.012.

[39] C. Chappard, A. Basillais, L. Benhamou, A. Bonassie, B.

Brunet-Imbault, N. Bonnet, and F. Peyrin, "Comparison of synchrotron radiation and conventional x-ray microcomputed tomography for assessing trabecular bone microarchitecture of human femoral heads," *Medical Physics*, vol. 33, Sep. 2006, pp. 3568–3577, DOI:10.1118/1.2256069.

[40] J. Van Dessel, Y. Huang, M. Depypere, I. Rubira-Bullen, F. Maes, and R. Jacobs, "A comparative evaluation of cone beam CT and micro-CT on trabecular bone structures in the human mandible," *Dentomaxillofacial Radiology*, vol. 42, Aug. 2013, p. 20130145, DOI:10.1259/dmfr.20130145.

[41] J. Gelb, D.P. Finegan, D.J.L. Brett, and P.R. Shearing, "Multi-scale 3D investigations of a commercial 18650 Li-ion battery with correlative electron- and X-ray microscopy," *Journal of Power Sources*, vol. 357, Jul. 2017, pp. 77–86, DOI:10.1016/j.jpowsour.2017.04.102.

[42] C.H. Arns, F. Bauget, A. Limaye, A. Sakellariou, T. Senden, A. Sheppard, R.M. Sok, V. Pinczewski, S. Bakke, L.I. Berge, P.E. Oren, and M.A. Knackstedt, "Pore Scale Characterization of Carbonates Using X-Ray Microtomography," *SPE Journal*, vol. 10, Dec. 2005, pp. 475–484, DOI:10.2118/90368-PA.

[43] S.J. Cooper, A. Bertei, P.R. Shearing, J.A. Kilner, and N.P. Brandon, "TauFactor: An open-source application for calculating tortuosity factors from tomographic data," *SoftwareX*, vol. 5, 2016, pp. 203–210, DOI:10.1016/j.softx.2016.09.002.

[44] J.C. Ferguson, F. Panerai, A. Borner, and N.N. Mansour, "PuMA: the Porous Microstructure Analysis software," *SoftwareX*, vol. 7, 2018, pp. 81–87, DOI:10.1016/j.softx.2018.03.001.

[45] J. Schindelin, I. Arganda-Carreras, E. Frise, V. Kaynig, M. Longair, T. Pietzsch, S. Preibisch, C. Rueden, S. Saalfeld, B. Schmid, J.Y. Tinevez, D.J. White, V. Hartenstein, K. Eliceiri, P. Tomancak, and A. Cardona, "Fiji: An open-source platform for biological-image analysis," *Nature Methods*, vol. 9, 2012, pp. 676–682, DOI:10.1038/nmeth.2019.

[46] J. Ollion, J. Cochennec, F. Loll, C. Escudé, and T. Boudier, "TANGO: a generic tool for high-throughput 3D image analysis for studying nuclear organization," *Bioinformatics*, vol. 29, Jul. 2013, pp. 1840–1841, DOI:10.1093/bioinformatics/btt276.

[47] D. Legland, I. Arganda-Carreras, and P. Andrey, "MorphoLibJ: Integrated library and plugins for mathematical morphology with ImageJ," *Bioinformatics*, vol. 32, 2016, pp. 3532–3534, DOI:10.1093/bioinformatics/btw413.

[48] S. BOLTE and F.P. CORDELIÈRES, "A guided tour into subcellular colocalization analysis in light microscopy," *Journal of Microscopy*, vol. 224, Dec. 2006, pp. 213–232, DOI:10.1111/j.1365-2818.2006.01706.x.

[49] J. Ahrens, B. Geveci, and C. Law, "ParaView: An End-User Tool for Large Data Visualization," *Visualization Handbook, Elsevier*, 2005, DOI:ISBN-13: 978-0123875822.

[50] M.P. Allen and D.J. Tildesley, *Computer Simulation of Liquids*, Oxford University Press, 1990, DOI:10.1093/oso/9780198803195.001.0001.

[51] J.G. Kirkwood and E.M. Boggs, "The Radial Distribution Function in Liquids," *The Journal of Chemical Physics*, vol. 10, Jun. 1942, pp. 394–402, DOI:10.1063/1.1723737.

[52] T. Aste, M. Saadatfar, and T. Senden, "Geometrical structure of disordered sphere packings," *Physical Review E*, vol. 71, Jun. 2005, p. 061302, DOI:10.1103/PhysRevE.71.061302.

[53] S. Franchetti, "Radial distribution functions in solid and liquid argon," *Il Nuovo Cimento B Series 11*, vol. 26, Apr. 1975, pp. 507–521, DOI:10.1007/BF02738574.

[54] B.J. Yoon, M.S. Jhon, and H. Eyring, "Radial distribution function of liquid argon according to significant structure theory," *Proceedings of the National Academy of Sciences*, vol. 78, Nov. 1981, pp. 6588–6591, DOI:10.1073/pnas.78.11.6588.

[55] B.A.F. Kopera and M. Retsch, "Computing the 3D Radial Distribution Function from Particle Positions: An Advanced Analytic Approach," *Analytical Chemistry*, vol. 90, 2018, pp. 13909–13914, DOI:10.1021/acs.analchem.8b03157.